IOP Publishing Physica Scripta
Phys. Scr. 95 (2020) 055506 (7pp) https://doi.org/10.1088/1402-4896/ab7681

Design and preparation of a single-band tunable metamaterial absorber in terahertz frequency

Min Zhong[1], **Xiaoting Jiang, Xuliang Zhu, Jing Zhang and Jinglin Zhong**

Hezhou University, Hezhou 542899, People's Republic of China

E-mail: zhongmin2012hy@163.com

Received 11 October 2019, revised 21 November 2019
Accepted for publication 14 February 2020
Published 26 February 2020

Abstract

A metamaterial-based absorber is designed and measured in the 13–16 THz range. An absorption peak of 93% amplitude is achieved at resonance frequency 14.2 THz, which is excited by the bright-bright modes coupling effect. In the first set of experiments, the structural parameter D is reduced from 26 μm to 25.6 μm, resulting in this absorption peak being enhanced from 93% to 97.2% and the resonance frequency moving from 142.THz to 14.65 THz. In the second set of experiments, the thickness of SU-8 layer is increased from 2 μm to 3 μm, resulting in this absorption peak being increased to 99.1% and the resonance frequency shifting 14.05 THz when the thickness of SU-8 layer is increased from 2 μm to 3 μm. When the incidence angle of electromagnetic wave reaches 75, up to 85% absorption rate is obtained. Since the STO layer reveals the temperature-dependent property, the resonance frequency can be controlled by changing the ambient temperature.

Keywords: metamaterials, absorption, temperature

(Some figures may appear in colour only in the online journal)

1. Introduction

Metamaterials with subwavelength scale units have attracted the attention of many researchers. This is because their unique properties that can't be found in nature, for example, negative index of refraction, lensing, and cloaking [1–7]. For example, a reported grapheme-based metamaterial device revealed the surface impedance properties different with natural materials [8]. Most of reported electromagnetic metamaterials structures contain metallic resonators, which leads to an inevitable loss of the electromagnetic wave energy. These energy absorption losses maybe degrades their performances. On the one hand, many structural design strategies are proposed to reduce this absorption loss, such as, optimizing the structure, using the gain materials to compensate loss, and using low loss materials, and so on [9–11]. On the other hand, the electromagnetic wave energy absorption loss can be leveraged to develop metamaterials absorbers. The first metamaterial absorber with a metallic cut wire and a split ring is proposed and verified by *Landy et al* [12], which revealed an absorption peak of 88%. Since then, high-performance electromagnetic absorber based on metamaterials are developed and validated in many frequency bands [13–15]. Since it can only be operated at a fixed frequency, many proven absorbers can't be used in industrial production. Therefore, tunable metamaterial absorbers have attracted researchers' attention. *Chen et al* reported a tunable metaferrite based on grapheme layer, which revealed resonance modes in the THz and IR bands [16]. Another multi-band metamaterial-based perfect absorber is proposed by Rasoul Alaee *et al* [17]. Many tunable strategies have been proposed and proved, such as photo excitation, electric stimuli, temperature, or MEMS [18–24]. To date, another temperature tunable dielectric layer, the strontium titanate (STO) layer, has received the attention of researchers. The dielectric constant of STO can be modulated in a continuous temperature spectrum.

In this paper, a single-band tunable metamaterial absorber is designed and measured in the 13–16 THz range. An absorption peak of 93% amplitude is achieved based on the

[1] Author to whom any correspondence should be addressed.

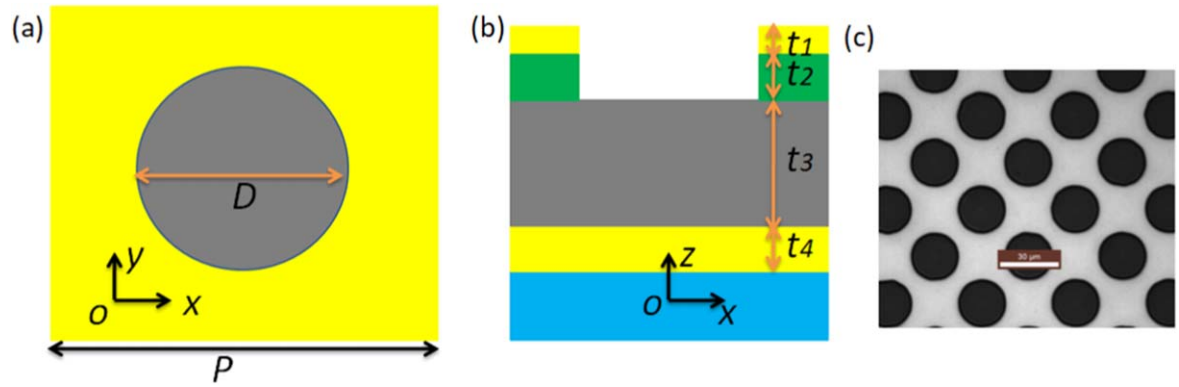

Figure 1. (a) The top view of unit cell. (b) The side view of unit cell. The yellow parts are metal layers. The gray part is SU-8 layer. The green part is STO layer. The blue part is substrate. (c) Sample photo.

Table 1. Geometric parameters.

Parameter	*P*	*D*	*t*1	*t*2	*t*3	*t*4
Value(μm)	30	26	0.055	0.1	2	0.1

bright-bright modes coupling effect at the resonance frequency 14.2 THz. Specifically, this absorption peak is shifted to higher frequencies and enhanced to 97.2% with the structural parameter D reducing, while it is shifted to lower frequencies and enhanced to 99.1% with the thickness of SU-8 layer increasiong. Moreover, the resonance frequency is shifted from 14.2 THz to 14.9 THz when the environment temperature is increased from 300 K to 380 k. Finally, up to 85% absorption rate can be obtained under incidence angle 75°.

2. Cell structure, model, and experiment

2.1. Unit structure and model

The designed unit cell can be found in figure 1. This unit cell contains four layers: the top metal layer is patterned with a round holes array. The second layer is a STO layer with the same array. The third layer is a complete SU-8 layer. The bottom layer is a complete metal layer. All of structure parameters can be found in table 1. In simulation, metal layers are given as follows:

$$\varepsilon(\omega) = 1 - \frac{\omega_P^2}{\omega^2 - i\omega\gamma_D} \tag{1}$$

In the equation above, $\gamma_D = 9 \times 10^{13}\,\mathrm{s}^{-1}$ is collision frequency, $\omega_p = 1.37 \times 10^{16}\,\mathrm{s}^{-1}$ is plasma frequency [25]. Simulations are revealed by the full-wave HFSS Ansoft. Floquet ports are used at top and bottom of the unit cell, and ideal electromagnetic boundary conditions are applied for sidewalls [26]. The permittivity of the STO layer is calculated as follows [27, 28]:

$$\varepsilon_w = \varepsilon_\infty + \frac{f}{w_o^2 - w^2 - iw\gamma} \tag{2}$$

In the above equation, ε_∞ is high-frequency bulk permittivity. $f = 2.6 \times 10^6\,\mathrm{cm}^{-2}$ is oscillator strength. The w_0 is soft mode frequency, which can be achieved as follows:

$$w_o(T)[\mathrm{cm}^{-1}] = \sqrt{31.2(T - 42.5)} \tag{3}$$

And the γ is soft mode damping factor, which can be revealed as follows:

$$\gamma(T)[\mathrm{cm}^{-1}] = -3.3 + 0.094\,\mathrm{T} \tag{4}$$

In above equation, T is ambient temperature.

2.2. Experiments

The samples are produced as follows: Before the experiments, a glass piece (cleaning and drying) is first selected as the substrate. Second, the bottom metal layer is deposited on the glass piece (Equipment device: ZZL-U400C). Third, the SU-8 will be spun on this metal layer (Equipment device: MSC-400Bz-6N spinner) and dried (Equipment device: C-MAG HP10). Fourth, the STO layer is deposited on the SU-8 layer (Equipment device: ZZL-U400C). Fifth, the top metal layer is deposited on the STO layer (Equipment device: ZZL-U400C). Sixth, the proposed array is defined through electron beam lithography (CABL-9000C) on the top metal layer.

3. Results and discussion

3.1. Physical mechanism of absorption peaks

The measured absorption spectrum is shown in figure 2. An absorption peak of 93% amplitude is achieved at the resonance frequency 14.2 THz. The simulated absorption spectrum is achieved by the HFSS, as shown in figure 2. In simulation, the transmission rate is zero due to the bottom metal layer is thick enough. The simulated reflection rate can be achieved based on the coupled mode theory (CMT), as follows [29–31]:

$$r = \frac{s_-}{s_+}\frac{j(\omega - \omega_o) + \delta - \gamma_e}{j(\omega - \omega_o) + \delta + \gamma_e} \tag{5}$$

$$A = 1 - |r|^2 = \frac{4\delta\gamma_e}{(\omega - \omega_o)^2 + (\delta + \gamma_e)^2} \tag{6}$$

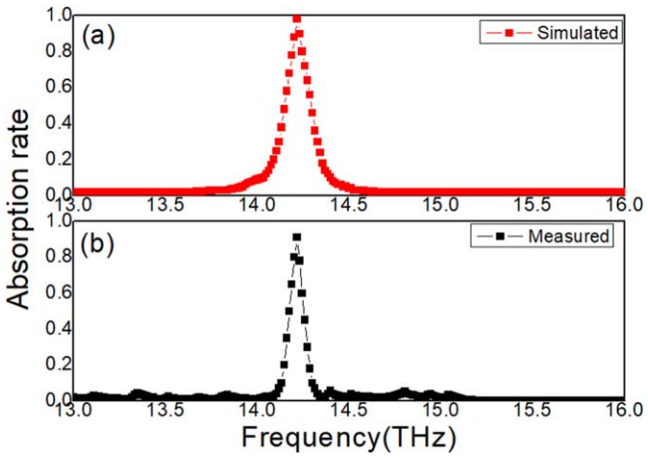

Figure 2. (a) Simulated absorption spectrum. (b) Measured absorption spectrum.

In this above equation, $s+$ and $s-$ are input and output waves of amplitudes. The δ is intrinsic loss rate. The γ_e is external leakage rate. The quality factor Q can be revealed as follows:

$$Q = \frac{f_o}{\Delta f} \tag{7}$$

Here, the f_o is the resonance frequency, and the Δf is the full width at half maximum (FWHM). Based on the measured results in figure 2, the total quality factor is Q = 142. To reveal the physical mechanism of this absorption peak, the electric field strength and current intensity are simulated at the resonance frequency 14.2 THz, as shown in figure 3. It is found that the current intensity is mainly concentrated on the surface of the top metal layer, as shown in figures 3(a), (b). Two bright modes are excited on the edges of the metal holes array, as shown in figures 3(c), (d). Moreover, the bright-bright modes coupling effect is also achieved, which results in the absorption peak at the resonance frequency 14.2 THz.

3.2. Influence of structural parameters

In the first set of experiments, the structural parameter D is set as 26 μm, 25.8 μm, and 25.6 μm, respectively (other structural parameters are unchanged). Figure 4 shows the measured absorption spectrum with different structural parameter D. It can be found that the absorption is enhanced from 93% to 97.2% by reducing the diameter of holes, as shown in figure 4. The resonance frequency of peak shows a blue shift from 14.2 THz to 14.65 THz for the change of 0.4 μm in the structural parameter D. In the second set of experiments, the thickness of SU-8 layer is set as 2 μm, 2.5 μm, and 3 μm, respectively (other structural parameters are also unchanged). The maximum peak absorption is enhanced from 93% to 99.1%, as shown in figure 5. The resonance frequency shows a red shift from 14.2 THz to 14.05 THz for the change of 1 μm in the structural parameter *t3*. The shift of resonance frequency is obviously smaller than that of figure 4.

To reveal the physical mechanism of these resonance behaviors in figures 4 and 5, an equivalent *LC* circuit model is proposed, as shown in figure 6. When electromagnetic waves are incident on the sample, the induced electric fields and current are achieved on the surface of metal layers. Two equivalent capacitances are also achieved based on these induced electric fields. Therefore, the equivalent *LC* circuit model can be given as follows [9, 32, 33]:

$$f = \frac{1}{2\pi\sqrt{(2L_1 + L_2) \cdot \dfrac{2C_1 \cdot C_2}{C_1 + 2C_2}}} \tag{8}$$

Here, the above formula can be simplified. This is because the majority induced current is excited on the surface of the top metal layer, and the equivalent capacitance C_2 is much higher than that of the equivalent capacitance C_1, which leads to the equivalent capacitance of the total sample is equal to C_1:

$$f \approx 2\pi\sqrt{C_1 \cdot (2L_1 + L_2)} \tag{9}$$

When the structural parameter D is reduced, the equivalent capacitance C_1 is increased synchronously. Therefore, the absorption peak is shifted to higher frequencies according to the equation (9). When the thickness of the SU-8 layer *t3* is increased, the vertical distance between the top and bottom metal layers is increased. The equivalent inductance L_2 in the bottom metal layer is reduced, which results in the reduction of the resonance frequency according to the equation (9).

3.3. Influence of temperature

The effect of temperature on the absorption peak is revealed in experiments. The measured absorption spectrum with different temperatures (D = 26 μm, and t3 = 2 μm) is shown in figure 7. The maximum absorption value is reduced from 93% to 90.4% with the ambient temperature increasing from 300 K to 380 K. Moreover, the resonance frequency of samples is shifted from 14.2 THz to 14.9 THz. The total frequency shift is 0.7 THz, which is corresponding to 80 K of temperature change. The resonance properties of the metal layers, the SU-8 layer, and the substrate are stable to temperature. This resonance frequency shift is directly related to the STO layer in samples. To understand this relationship, the permittivity and loss tangent of the STO layer are calculated under different temperature conditions, as shown in figure 8. When the temperature is increased, the real part of permittivity of the STO layer is reduced significantly, as shown in figure 8(a), which is also consistent with the equation (2). Based on the perturbation theory, the resonance frequency shift of samples due to the material perturbation of STO layer can be given as follows [34–36]:

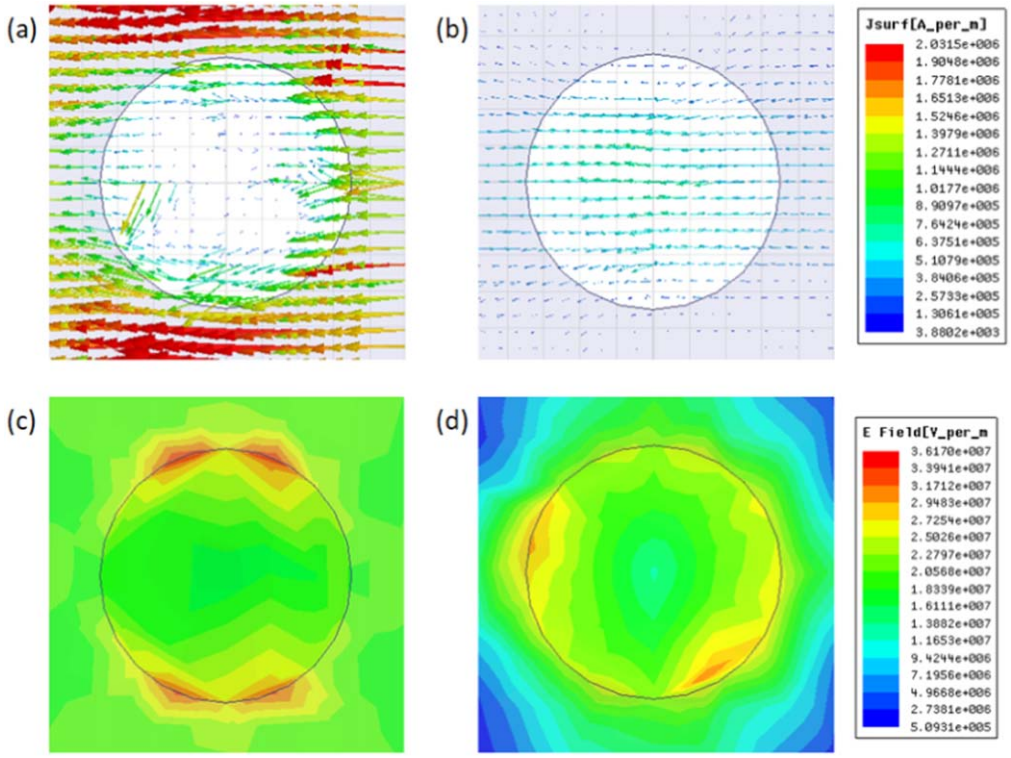

Figure 3. (a) The simulated current intensity on the surface of the top metal layer at resonance frequency 14.2 THz. (b) The simulated current intensity on the surface of the bottom metal layer at resonance frequency 14.2 THz. (c) The simulated electric field strength on the surface of the top metal layer at resonance frequency 14.2 THz. (d) The simulated electric field strength on the surface of the bottom metal layer at resonance frequency 14.2 THz.

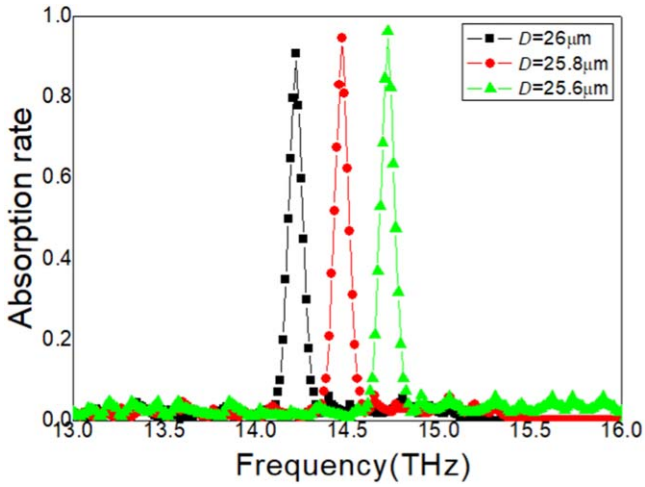

Figure 4. The measured absorption spectrum with different structural parameter *D*.

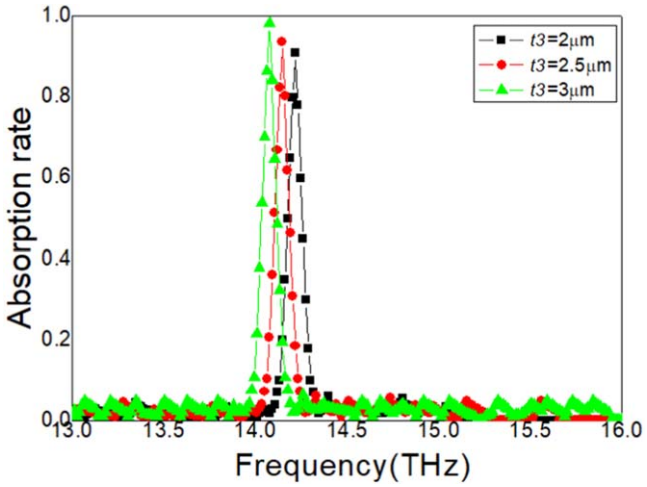

Figure 5. The measured absorption spectrum with different structural parameter t3.

$$\frac{\Delta\omega}{\omega} = \frac{\omega - \omega_o}{\omega_o} \approx \frac{-\iiint_V [(\Delta\vec{\varepsilon}\cdot\vec{E})\cdot\vec{E}_o^{*} + (\Delta\vec{\mu}\cdot\vec{H})\cdot\vec{H}_o]dV}{\iiint (\varepsilon\,|\vec{E}_o|^2 + \mu\,|\vec{H}_o|^2)dV} \quad (10)$$

Where, the $\Delta\vec{\varepsilon}$ is the change of permittivity of the STO layer and $\Delta\vec{\mu}$ is the change of permittivity of the STO layer. The $\vec{E}_o$ and $\vec{H}_o$ are the unperturbed electric and magnetic fields, respectively. The $\vec{E}$ and $\vec{H}$ are the perturbed electric and magnetic fields, respectively. As the temperature increases, the real part of the permittivity is reduced, which results in a $\Delta\vec{\varepsilon}$ less than zero. Moreover, the resonance frequency of samples is increased according to the equation (10). Therefore, the absorption peak is shifted to higher frequencies in figure 7. On the other hand, the loss tangent of the STO layer

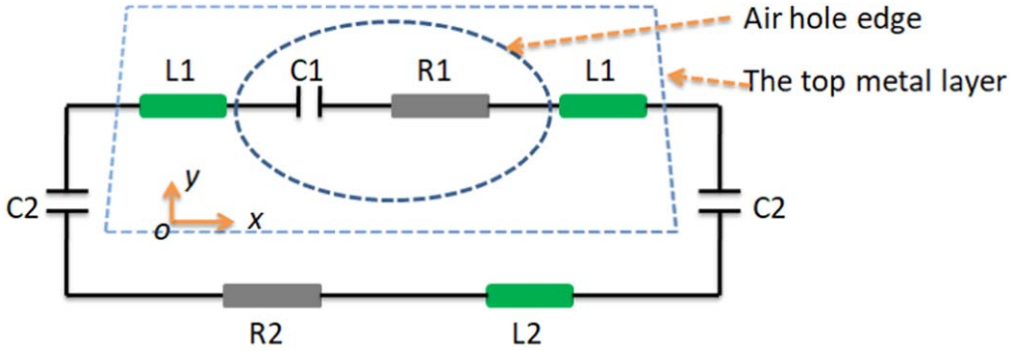

Figure 6. Equivalent *LC* circuit model of unit cell.

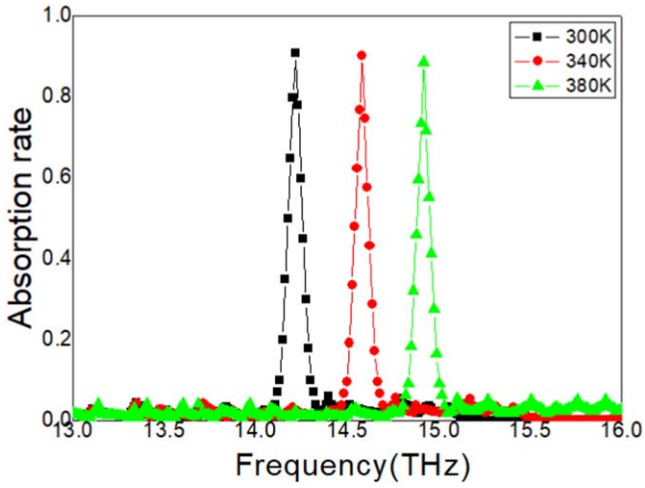

Figure 7. The measured absorption spectrum with different temperatures.

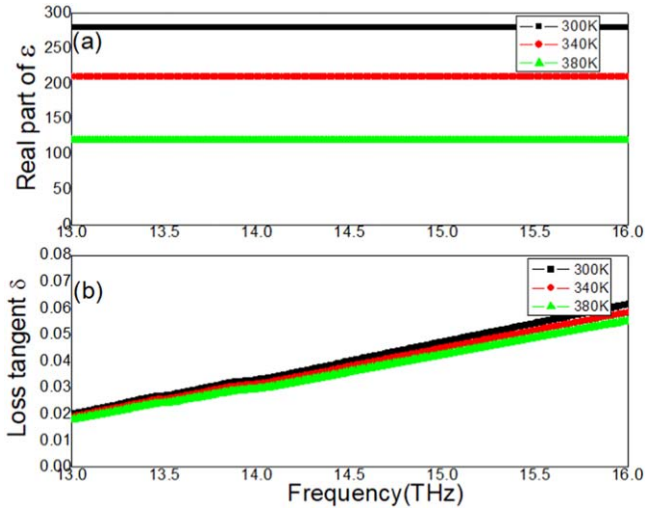

Figure 8. (a) The real part of permittivity of the STO layer with different temperature. (b) The loss tangent of the STO layer with different temperature.

is reduced with the temperature increasing, which leads to the dielectric loss of electromagnetic energy in the STO layer reduce and the absorption peak reduce synchronously.

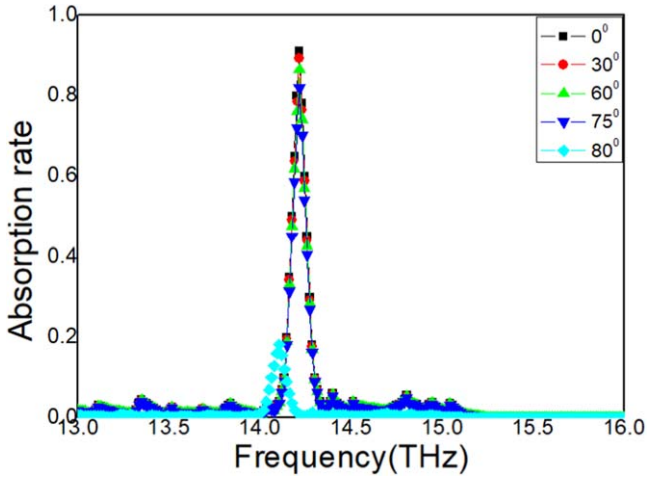

Figure 9. The measured absorption spectrum with different incidence angles.

3.4. Influence of incident angle

The absorption stabilities of samples with oblique incidence angles are also measured. The measured absorption spectrum is shown in figure 9 ($D = 26\ \mu$m, t3 $= 2\ \mu$m, and T $=$ 300 K). The resonance frequency of the absorption peak is almost unchanged with the incidence angle incresing from 0° to 75°. When the incidence angle is increased to 80°, the resonance frequency is shifted to the lower frequency 14.1 THz, as shown in figure 9. The maximum absorption is larger than 85% when the incidence angle is lower than 75°. However, when the incidence angle is increased to 80°, the maximum absorption is abnormally reduced. Therefore, the high absorption performance can be obtained when the incidence angle is lower than 75°. To reveal the abnormally reduction of the absorption peak in figure 9, the electric field strength distribution is calculated at the resonance frequency point 14.1 THz, as shown in figure 10. Only one bright mode is excited in the top layer, and no bright mode can be excited in the bottom metal, as shown in figure 10(a). The resonance intensity of this bright mode is so weakly, far below the results of figure 3(c). Moreover, the coupling between bright-bright modes can't be found, which leads to the abnormally reduction of the absorption peak. This is because the absorption peak is derived from the resonance and coupling

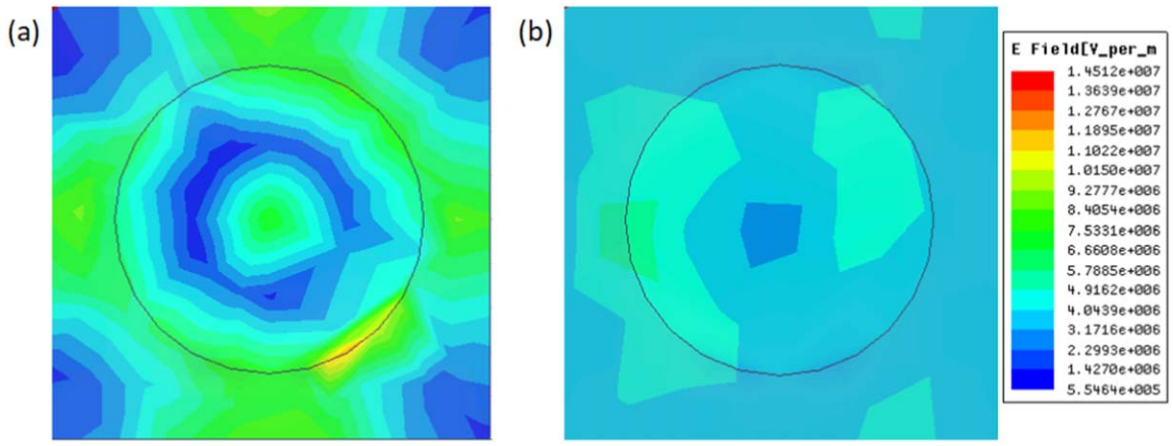

Figure 10. The simulated electric field strength distribution at the resonance frequency point 14.1 THz. (a)The top metal layer. (b) The bottom metal layer.

of bright modes, as shown in figure 3. When the incidence angle is larger than 80°, the coupling effect between the electromagnetic wave and the induced electric field is failed. As a result, these bright modes are not to be effectively activated, as shown in figure 10.

4. Conclusion

In conclusion, a single-band tunable metamaterial absorber is demonstrated in the 13–16 THz range. The absorption peak (93% amplitude) is excited by the bright-bright modes coupling effect at the resonance frequency 14.2 THz. The effect of the structural parameters (*D* and *t3*) on the absorption peak is revealed in experiments. The absorption peak is tunable through changing the structure parameters individually. High absorption performance (up to 85%) is obtained under the incidence angle 75°. Since the permittivity of the STO layer is sensitive to the temperature change, this absorption peak is tunable by changing the ambient temperature. The resonance frequency is shifted from 14.2 THz to 14.9 THz with the environment temperature increasing from 300 K to 380 k.

Acknowledgments

This research was financially supported by the Doctor's Scientific Research Foundation (No. HZUBS201503), the Young and Middle Teachers' Basic Ability Improvement Project of Guangxi (No. KY2016YB453), the Mathematical Support Autonomous Discipline Project of Hezhou University (No. 2016HZXYSX01), and the Innovation and Entrepreneurship Students Project of Hezhou University (Nos. 201611838018, 201911838062, 201911838071, 201911838179).

ORCID iDs

Min Zhong https://orcid.org/0000-0002-0301-8324

References

[1] Schurig D, Mock J J, Justice B J, Cummer S A, Pendry J B, Starr A F and Smith D R 2006 Metamaterial electromagnetic cloak at microwave frequencies *Science* **314** 977–80
[2] Liu C, Liu P, Yang C, Lin Y and Liu H 2019 Analogue of dual-controlled electromagnetically induced transparency based on graphene metamaterial *Carbon* **142** 354–62
[3] Sun D, Wu Z-K, Divin C, Li X, Berger C, Deheer W A, First P N and Norris T B 2008 Ultrafast relaxation of excited Dirac fermions in epitaxial graphene using optical differential transmission spectroscopy *Phys. Rev. Lett.* **101** 157402
[4] He X, Yao Y, Yang X, Lu G, Yang W, Yang Y, Wu F, Yu Z and Jiang J 2018 Dynamically controlled electromagnetically induced transparency in terahertz graphene metamaterial for modulation and slow light applications *Opt. Commun.* **410** 206–10
[5] Smith D R, Pendry J B and Wiltshire M C K 2004 Metamaterials and negative refractive index *Science* **305** 788–92
[6] Liang T, Gibson Q, Ali M, Liu M, Cava R J and Ong N P 2015 Ultrahigh mobility and giant magnetoresistance in the Dirac semimetal Cd3As2 *Nat. Mater.* **14** 280–4
[7] Badioli M, Woessner A, Tielrooij K J, Nanot S, Navickaite G, Stauber T, Garcia de Abajo F J and Koppens F H L 2014 Phonon-mediated mid-Infrared photoresponse of graphene *Nano Lett.* **14** 6374–81
[8] Chen P Y and Alu A 2013 Terahertz metamaterial devices based on graphene nanostructures *IEEE Trans. Terahertz Science and Technology* **3** 748–56
[9] Zhou J, Koschny T and Soukoulis C M 2008 An efficient way to reduce losses of left-handed metamaterials *Opt. Express* **16** 11147–52
[10] Boltasseva A and Atwater H A 2011 Low-less plasmonic metamaterials *Science* **331** 290–1
[11] Wuestner S, Pusch A, Tsakmakidis K L, Hamm J M and Hess O 2010 Overcoming losses with gain in a negative refraction index metamaterials *Phys. Rev. Lett.* **105** 127401
[12] Landy N I, Sajuyigbe S, Mock J J, Smith D R and Padilla W J 2008 Perfect metamaterial absorber *Phys. Rev. Lett.* **100** 207402
[13] Song Z, Wang K, Li J and Liu Q H 2018 Broadband tunable terahertz absorber based on vanadium dioxide metamaterials *Opt. Express* **26** 7148–54

[14] Luo M, Shen S, Zhou L, Wu S, Zhou Y and Chen L 2017 Broadband, wide-angle, and polarization-independent metamaterial absorber for the visible regime *Opt. Express* **25** 16715–24
[15] Xu J *et al* 2016 Design of tripleband metamaterial absorbers with refractive index sensitivity at infrared frequencies *Opt. Express* **24** 25742–51
[16] Chen P Y, Farhat M and Bağcı H 2015 Graphene metascreen for designing compact infrared absorbers with enhanced bandwidth *Nanotechnology* **26** 164002–10
[17] Alaee R, Farhat M, Rockstuhl C and Lederer F 2012 A perfect absorber made of a graphene microribbon metamaterial *Opt. Express* **20** 28017
[18] Yin X, Schäferling M, Michel A-K U, Tittl A, Wuttig M, Taubner T and Giessen H 2015 Active chiral plasmonics *Nano Lett.* **15** 4255–60
[19] Zhu W M, Liu A Q, Bourouina T, Tsai D P, Teng J H, Zhang X H, Lo G Q, Kwong D L and Zheludev N I 2012 Microelectromechanical Maltese-cross metamaterial with tunable terahertz anisotropy *Nat. Commun.* **3** 1274
[20] Liu M *et al* 2012 Terahertz-field-induced insulator-to-metal transition in vanadium dioxide metamaterial *Nature* **487** 345–8
[21] Buchnev O, Podoliak N, Kaczmarek M, Zheludev N I and Fedotov V A 2015 Electrically controlled nanostructured metasurface loaded with liquid crystal: toward multifunctional photonic switch *Adv. Optical Mater.* **3** 674–9
[22] Lv T, Zhu Z, Shi J, Guan C, Wang Z P and Cui T J 2014 Optically controlled background-free terahertz switching in chiral metamaterial *Opt. Lett.* **39** 3066–9
[23] Zhou J, Chowdhury D R, Zhao R, Azad A K, Chen H, Soukoulis C M, Taylor A J and Hara J F O 2012 Terahertz chiral metamaterials with giant and dynamically tunable optical activity *Phys. Rev.* B **86** 035448
[24] Miao Z, Wu Q, Li X, He Q, Ding K, An Z, Zhang Y and Zhou L 2014 Widely tunable terahertz phase modulation with gate-controlled graphene metasurfaces *Phys. Rev.* X **5** 041027
[25] Zhang S, Fan W J, Paniou N C, Malley K J, Osgood R M and Brueck S R J 2005 Optical negative-index bulk metamaterials consisting of 2D perforated metaldielectric stacks *Phys. Rev. Lett.* **95** 137404
[26] Smith D R, Schult S, Markos P and Soukoulis C M 2002 Determination of effective permittivity and permeability of metamaterials from reflection and transmission coefficients *Phys.Rev.* B **65** 195104–8
[27] Kuzel P and Kadlec F 2008 Tunable structures and modulators for THz light *C. R. Physique* **9** 197–214
[28] Nemec H, Kuzel P, Duvillaret L, Pashkin A, Dressel M and Sebastian M T 2005 Highly tunable photonic crystal filter for the terahertz range *Opt. Lett.* **30** 549–51
[29] Jiang X, Wang T, Xiao S, Yan X and Cheng L 2017 Tunable ultra-high-efficiency light absorption of monolayer graphene using critical coupling with guided resonance, *Opt. Express* **25** 27028–36
[30] Piper J R and Fan S 2014 Total absorption in a graphene monolayer in the optical regime by critical coupling with a photonic crystal guided resonance *ACS Photonics* **1** 347–53
[31] Li H, Qin M, Wang L, Zhai X, Ren R and Hu J 2017 Total absorption of light in monolayer transition-metal dichalcogenides by critical coupling *Opt. Express* **25** 31612–21
[32] Zhou J, Economon E N, Koschny T and Soukoulis C M 2006 Unifying approach to left-handed material design *Opt. Lett.* **31** 3620–2
[33] Pang Y, Cheng H, Zhou Y and Wang J 2013 Analysis and design of wirebased metamaterial absorbers using equivalent circuit approach *J. Appl. Phys.* **113** 114902
[34] Li Z and Yu N 2013 Modulation of mid-infrared light using graphene-metal plasmonic antennas *Appl. Phys. Lett.* **102** 131108
[35] Yao Y, Kats M A, Genevet P, Yu N, Song Y, Kong J and Capasso F 2013 Broad electrical tuning of grapheneloaded plasmonic antennas *Nano Lett.* **13** 1257–64
[36] Hwang J and Roh J W 2017 Electrically tunable two-dimensional metasurfaces at near-infrared wavelengths *Opt. Express* **25** 25071–8